

Testing *CPT* and Lorentz symmetry with hydrogen masers

M. A. Humphrey, D. F. Phillips, E. M. Mattison, R. F. C. Vessot, R. E. Stoner, and R. L. Walsworth
Harvard-Smithsonian Center for Astrophysics, Cambridge, Massachusetts 02138, USA
(Received 4 August 2003; published 9 December 2003)

In a recent paper [Phys. Rev. D **63**, 111101 (2001)] we reported a new limit on *CPT* (charge, parity, and time reversal) and Lorentz violation of the proton by using a hydrogen maser to search for a sidereal variation of the $F=1$, $\Delta m_F = \pm 1$ Zeeman frequency in atomic hydrogen. Here we discuss the theoretical interpretation of this recent experiment, the operating principles of the maser, and the double-resonance technique used to measure the Zeeman frequency. We also describe the characterization of systematic effects and details of the data analysis. We conclude by comparing our result to other recent experiments, and discussing potential improvements to the hydrogen maser double-resonance technique.

DOI: 10.1103/PhysRevA.68.063807

PACS number(s): 42.62.Eh, 06.30.Ft, 11.30.Cp, 11.30.Er

I. INTRODUCTION

A theoretical framework has been developed by Kostelecký and co-workers [1–5] which incorporates possible violation of Lorentz symmetry and *CPT* (charge, parity, and time reversal) into a realistic extension of the standard model of elementary particle physics. One branch of this framework emphasizes low-energy, experimental searches for symmetry violating effects in atomic energy levels [4,5]. In particular, it has been shown that Lorentz and *CPT* violation results in variations in the atomic hydrogen $F=1$, $\Delta m_F = \pm 1$ Zeeman frequency as a function of the orientation of the quantization axis (set by a static magnetic field) relative to a preferred frame (e.g., the cosmic microwave background) [6]. Motivated by this theoretical framework, we used a hydrogen maser double-resonance technique to search for variations in the hydrogen Zeeman frequency with a period of the sidereal day (23.93 h), and placed a new, clean bound of $\approx 10^{-27}$ GeV on Lorentz and *CPT* violation of the proton [7].

Here we provide details of the theoretical framework, experiment, and analysis, which underlie our recent hydrogen maser test of *CPT* and Lorentz symmetry. In Secs. II and III we review the theoretical framework. In Sec. IV we describe the basic concepts of hydrogen maser operation and our double-resonance Zeeman frequency measurement technique. In Sec. V we discuss the procedure used to collect data and extract a sidereal bound on the Zeeman frequency. In Sec. VI we describe efforts to reduce and characterize systematic effects. Finally, in Sec. VII we compare our result to other clock-comparison tests of *CPT* and Lorentz symmetry, and discuss potential means of improving our measurement.

II. LORENTZ AND *CPT* VIOLATION IN THE STANDARD MODEL EXTENSION

Experimental investigations of Lorentz symmetry provide important tests of the standard model of particle physics as well as general relativity. While the standard model successfully describes particle phenomenology, it is believed to be the low-energy limit of a fundamental theory that incorporates gravity. This underlying theory may be Lorentz invariant, yet contain spontaneous symmetry breaking that could

result in small violations of Lorentz invariance and hence *CPT* at the level of the standard model [1].

A theoretical framework has been developed by Kostelecký and co-workers to describe Lorentz and *CPT* violation at the level of the standard model [1–5]. This standard model extension is quite general: it emerges as the low-energy limit of any underlying theory that generates the standard model and contains spontaneous Lorentz symmetry violation, and hence can include *CPT* violation [1]. For example, such characteristics might emerge from string theory [2]. A key feature of the standard model extension is that it is formulated at the level of the known elementary particles, and thus enables quantitative comparison of a wide array of searches for Lorentz and *CPT* violation [3].

In the standard model extension, Lorentz and *CPT* violating terms are included in the relativistic Lagrange density of the constituent particles of the atom. For example, the modified electron Lagrangian becomes [4]

$$\mathcal{L} = \frac{1}{2} i \bar{\psi} \Gamma_\nu \partial^\nu \psi - \bar{\psi} M \psi, \quad (1)$$

where

$$\Gamma_\nu = \gamma_\nu + (c_{\mu\nu} \gamma^\mu + d_{\mu\nu} \gamma_5 \gamma^\mu) \quad (2)$$

and

$$M = m + (a_\mu \gamma^\mu + b_\mu \gamma_5 \gamma^\mu + \frac{1}{2} H_{\mu\nu} \sigma^{\mu\nu}). \quad (3)$$

The parameters a_μ , b_μ , $c_{\mu\nu}$, $d_{\mu\nu}$, and $H_{\mu\nu}$ each represent the product of vacuum expectation values of Lorentz tensors (e.g., generated through spontaneous Lorentz symmetry breaking in an underlying theory) and coupling strengths to the electron field. All these parameters are absent in the standard model [8]. *CPT* and Lorentz symmetry are violated by a_μ and b_μ , while $c_{\mu\nu}$, $d_{\mu\nu}$, and $H_{\mu\nu}$ violate Lorentz symmetry only. An analogous expression exists for the modified proton and neutron Lagrangians (a superscript will be appended to differentiate between the sets of parameters for different particle types). The standard model extension modifies only the free particle properties of constituent systems (nuclei, atoms, etc.), as all Lorentz-violating interaction effects will be of higher order [4]. Since both the particle field ψ and the background expectation values transform covari-

TABLE I. Experimental bounds on Lorentz and *CPT* violation for the electron, proton, and neutron in terms of the parameters $\tilde{b}_X = b_X - m_e d_{X0} - H_{YZ}$ and $\tilde{b}_Y = b_Y - m_e d_{Y0} - H_{ZX}$, where the subscripts denote the projection of the tensor couplings onto a fixed inertial frame (see Sec. VII). Bounds are listed by order of magnitude and in terms of a sum of Lorentz-violating parameters in the standard model extension [see Eqs. (2)–(4)].

| Experiment | $\tilde{b}_{X,Y}^e$ (GeV) | $\tilde{b}_{X,Y}^p$ (GeV) | $\tilde{b}_{X,Y}^n$ (GeV) |
|---|---------------------------|---------------------------|---------------------------|
| Anomaly frequency of e^- in Penning trap [10] | 10^{-25} | | |
| ^{199}Hg and ^{133}Cs precession frequencies [14] | 10^{-27} | 10^{-27} | 10^{-30} |
| Hydrogen maser double resonance [7] | 10^{-27} | 10^{-27} | |
| Spin-polarized torsion pendulum [12] | 10^{-29} | | |
| Dual species $^{129}\text{Xe}/^3\text{He}$ maser [13] | | | 10^{-31} |

antly, the Lagrangian [Eq. (1)] remains invariant under observer Lorentz transformations. However, the background expectation values are unaffected by particle Lorentz transformations, leading to nontrivial changes in the theory under rotations and boosts [4].

Within this framework alone, the values of the parameters that characterize Lorentz violation are not calculable; instead, values or constraints must be determined experimentally. The general nature of this theory ensures that bounds placed on different combinations of Lorentz and *CPT* violating terms may be compared between different experiments (see Table I and Ref. [4]).

For example, Lorentz and *CPT* violation may produce shifts in atomic levels depending on the orientation of the constituent particles' spins relative to some unknown, fixed inertial frame [4,5]. (Boosts relative to the preferred inertial frame may also cause atomic energy level shifts [9].) Certain atomic transition frequencies, therefore, may exhibit sinusoidal variation as the Earth rotates on its axis. Sensitive tests of Lorentz and *CPT* symmetry can be made by searching for sidereal variation of these atomic transition frequencies.

As shown in Table I, among the most sensitive such experiments are Penning trap tests by Dehmelt and co-workers with the electron and positron [10] which place a limit on electron Lorentz and *CPT* violation at a level of $\approx 10^{-25}$ GeV. A recent reanalysis by Adelberger, Gundlach, Heckel, and co-workers of existing data from the “Eöt-Wash II” spin-polarized torsion pendulum [11] has improved this limit to a level of $\approx 10^{-29}$ GeV [12], the most stringent bound to date on Lorentz and *CPT* violation of the electron. A limit on neutron Lorentz and *CPT* violation of about 10^{-31} GeV has been set by Bear *et al.* [13] using a dual species noble gas maser to compare the nuclear Zeeman frequencies of ^{129}Xe and ^3He . Stringent limits on Lorentz and *CPT* violation of the electron, proton, and neutron have also been derived [4] from the results of an experiment by Berglund *et al.* [14] which compared the Zeeman frequencies of ^{199}Hg and ^{133}Cs .

III. APPLICATION OF THE STANDARD MODEL EXTENSION TO ATOMIC HYDROGEN HYPERFINE/ZEEMAN ENERGY LEVELS

Atomic energy-level shifts due to Lorentz violation are calculated perturbatively using standard field-theory tech-

niques by taking the expectation value of the Hamiltonian derived from the standard model extension’s modified Lagrangian. Note that for most atoms, the interpretation of energy-level shifts in terms of the standard model extension is reliant on the particular model used to describe the atomic nucleus (e.g., the Schmidt model). A key advantage of an experimental study in atomic hydrogen is the simplicity of the nuclear structure (a single proton), with results that are therefore “clean,” i.e., uncompromised by any nuclear model uncertainty.

Figure 1 illustrates the Lorentz-violating corrections to the hyperfine/Zeeman energy levels of the ground electronic state of atomic hydrogen [6]. In particular, the shift in the $F=1$, $\Delta m_F = \pm 1$ Zeeman frequency, following the notation of Refs. [4–7], is

$$|\Delta \nu_Z| = \frac{1}{h} |\tilde{b}_z^e + \tilde{b}_z^p|, \quad (4)$$

where $\tilde{b}_z^w = b_z^w - d_{zt}^w m_w - H_{xy}^w$ for $w = p$ or e^- [8]. The spatial subscripts (x , y , z) denote the projection of the tensor cou-

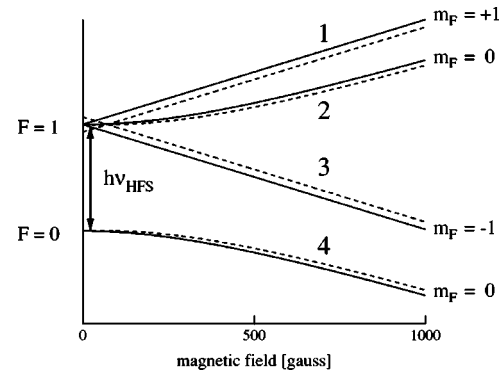


FIG. 1. Hydrogen hyperfine/Zeeman energy levels. The full curves are the unperturbed levels, while the dashed curves illustrate the shifts due to Lorentz and *CPT* violating effects for the exaggerated values of $|b_z^e - d_{zt}^e m_e - H_{xy}^e| = 90$ MHz and $|b_z^p - d_{zt}^p m_p - H_{xy}^p| = 10$ MHz. (We have set a bound of less than 1 mHz for these terms [7].) A hydrogen maser typically oscillates on the first-order magnetic-field-independent $|2\rangle \leftrightarrow |4\rangle$ hyperfine transition near 1420 MHz, and with a static magnetic field of less than 1 mG. For these low field strengths, the two $F=1$, $\Delta m_F = \pm 1$ Zeeman frequencies are nearly degenerate, and $\nu_{12} \approx \nu_{23} \approx 1$ kHz.

plings onto the laboratory frame, where z is the quantization axis of the hydrogen atoms, and t is the time subscript. Therefore, as the Earth rotates relative to a fixed inertial frame, the Zeeman frequency ν_Z will exhibit a sidereal variation. Our recent search for a variation of the hydrogen $F=1$, $\Delta m_F=\pm 1$ Zeeman frequency using hydrogen masers has placed a new, clean bound on Lorentz and *CPT* violation of the proton at a level of about 10^{-27} GeV [7].

IV. HYDROGEN MASER CONCEPTS AND OPERATION

The electronic ground state of hydrogen is split into four levels by the hyperfine interaction, labeled (following the notation of Andresen [15]) as $|1\rangle$ to $|4\rangle$ in order of decreasing energy (Fig. 1). In low magnetic fields, the energies of states $|2\rangle$ and $|4\rangle$ have only a second-order field dependence. Therefore, a hydrogen maser is typically designed to oscillate on the $|2\rangle \leftrightarrow |4\rangle$ transition. This transition frequency (in hertz) as a function of static magnetic field (in gauss) is given by $\nu_{24} = \nu_{hfs} + 2750B^2$, where $\nu_{hfs} \approx 1420.405\,751$ MHz is the zero-field hyperfine frequency. Hydrogen masers typically operate with low static fields (less than 1 mG), such that the two $F=1$, $\Delta m_F=\pm 1$ Zeeman frequencies, given by $\nu_{12}=1.4\times 10^6 B - 1375B^2$ and $\nu_{23}=1.4\times 10^6 B + 1375B^2$, are nearly degenerate. For example, at $B=0.5$ mG, $\nu_{12}-\nu_{23} \approx 1$ mHz, which is much less than the typical Zeeman linewidth of ≈ 1 Hz. We refer to both ν_{12} and ν_{23} as ν_Z when their splitting is not significant.

A. Maser operation

In a hydrogen maser [16–18], molecular hydrogen is dissociated in a rf discharge and a thermal beam of hydrogen atoms is formed, as shown schematically in Fig. 2. A hexapole state selecting magnet focuses the low-field-seeking hyperfine states $|1\rangle$ and $|2\rangle$ into a quartz maser bulb at about 10^{12} atoms/s. Inside the bulb (volume $\sim 10^3$ cm 3), the atoms travel ballistically for about 1 s before escaping, making $\sim 10^4$ collisions with the bulb wall. A Teflon coating reduces the atom-wall interaction and thus inhibits decoherence of the masing atomic ensemble due to wall collisions. The maser bulb is centered inside a cylindrical TE₀₁₁ microwave cavity resonant with the 1420-MHz hyperfine transition. The thermal microwave field stimulates a coherent magnetization in the atomic ensemble, and this magnetization acts as a source to stimulate the cavity microwave field. With sufficiently high atomic flux and low cavity losses, this feedback induces active maser oscillation. The maser signal (typically about 10^{-13} W) is inductively coupled out of the microwave cavity, amplified, and detected with a low noise heterodyne receiver. A solenoid surrounding the cavity produces a weak static magnetic field (≈ 1 mG) which establishes the quantization axis inside the maser bulb and sets the Zeeman frequency (≈ 1 kHz). A pair of coils oriented orthogonal to the cavity axis can be used to produce an oscillating transverse magnetic field to drive the $F=1$, $\Delta m_F=\pm 1$ Zeeman transitions. The cavity, solenoid, and Zeeman coils are all enclosed within four layers of high permeability magnetic shielding

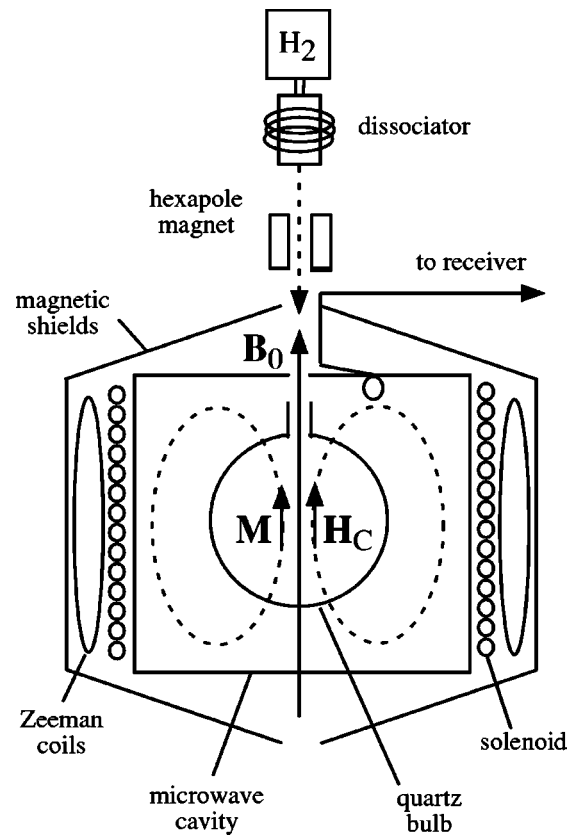


FIG. 2. Hydrogen maser schematic. The solenoid generates a weak static magnetic field \mathbf{B}_0 which defines a quantization axis inside the maser bulb. The microwave cavity field \mathbf{H}_C (dashed field lines) and the coherent magnetization \mathbf{M} of the atomic ensemble form the coupled actively oscillating system.

and temperature controlled (typically at about 320 K) to about 0.1 mK by a four-stage system of enclosures.

A well engineered hydrogen maser can have a fractional frequency stability $\approx 10^{-13}/\sqrt{\tau}$ over intervals τ of seconds to hours limited by thermal noise and spin-exchange collisions [18]. This high stability is enabled by a long atom-field interaction time (1 s), first-order independence of the atomic transition frequency on magnetic field (at the low operating fields), a weak atom-wall interaction (due to the low atomic polarizability of H and the wall's Teflon coating), reduced Doppler effects (the atoms are confined to a region of uniform microwave field phase, effectively averaging their velocity to zero over the interaction time with the field), and multiple layers of thermal control of the cavity (stabilizing cavity pulling frequency shifts).

B. Maser characterization

Among the quantities used to characterize a hydrogen maser, those most relevant to the double-resonance *CPT*/Lorentz symmetry test are the atomic line quality factor Q_1 , the population difference decay rate γ_1 , the hyperfine decoherence rate γ_2 , the atomic flow rate into and out of the bulb γ_b , and the maser Rabi frequency $|X_{24}|$. In Table II we present the results of a comprehensive set of measurements characterizing these and other parameters for one of the hy-

TABLE II. Operational parameters for masers P-8 and P-28 (*in SI units*). Parameter values in regular type were either measured directly (e.g., output power P_o), calculated from first principles or geometric measurements (e.g., filling factor η and bulb escape rate γ_b), or derived from line- Q and power measurements as described in Sec. IV B. Parameter values given in italics were determined from double-resonance measurements as described in Sec. V A. The values of $|X_{12}|$ and γ_Z for P-8 were determined from Eq. (20) using values for γ_1 , γ_2 , γ_b , and $|X_{24}|$. The value of $|X_{12}|$ for P-28 was set such that the ratio of the square of $|X_{12}|$ for P-28 to that for P-8 was equal to the ratio of the measured amplitudes of double-resonance-induced maser frequency shifts.

| Parameter | Symbol | P-8 | P-28 |
|----------------------------------|---------------|--|----------------------------------|
| Cavity volume | V_C | $1.4 \times 10^{-2} \text{ m}^3$ | $1.4 \times 10^{-2} \text{ m}^3$ |
| Bulb volume | V_b | $2.9 \times 10^{-3} \text{ m}^3$ | $2.9 \times 10^{-3} \text{ m}^3$ |
| Filling factor | η | 2.14 | 2.14 |
| Bulb escape rate | γ_b | 0.86 rad/s | 0.86 rad/s |
| Cavity- Q (quality factor) | Q_C | 39 300 | 39 400 |
| Cavity coupling coefficient | β | 0.23 | 0.25 |
| Line- Q (quality factor) | Q_l | 1.6×10^9 | 1.9×10^9 |
| Output power | P_o | 110 fW | 75 fW |
| Radiated power | P | 600 fW | 400 fW |
| Maser quality parameter | q | 0.05 | |
| One-body relax. rate | γ_t | 1.7 rad/s | |
| Threshold power | P_c | 220 fW | |
| Threshold flux | I_{th} | $0.5 \times 10^{12} \text{ atoms/s}$ | |
| Inverted population flux | I | $2.1 \times 10^{12} \text{ atoms/s}$ | |
| Total atomic flux | I_{tot} | $5 \times 10^{12} \text{ atoms/s}$ | |
| Atomic density | n | $1.0 \times 10^{15} \text{ atoms/m}^3$ | |
| Spin-exchange rate | γ_{se} | 0.4 rad/s | |
| Maser decoherence rate | γ_2 | 2.8 rad/s | 2.3 rad/s |
| Zeeman Rabi frequency | $ X_{12} $ | 0.9 rad/s | 0.3 rad/s |
| Zeeman decoherence rate | γ_Z | 2.4 rad/s | 2.4 rad/s |
| Maser Rabi frequency | $ X_{24} $ | 2.9 rad/s, 2.2 rad/s | 2.1 rad/s |
| Population difference decay rate | γ_1 | 2.0 rad/s, 1.3 rad/s | 1.1 rad/s |

drogen masers in our laboratory, referred to as P-8. Table II also includes a more restricted set of parameters for maser P-28 [19], the maser used in our recent *CPT/Lorentz symmetry test* [7]. In the remainder of this section we describe the operational parameters that are specific to these hydrogen masers [20].

The filling factor, defined as [17,18]

$$\eta = \frac{\langle H_z \rangle_{bulb}^2}{\langle H^2 \rangle_{cavity}}, \quad (5)$$

quantifies the ratio of the energy of the average microwave magnetic-field component that couples to the atoms inside the maser bulb, to the average total microwave magnetic-field energy in the cavity.

There are two hydrogen maser relaxation rates: the population difference decay rate γ_1 and the hyperfine decoherence rate γ_2 . In a standard H maser as described above, the population decay is given by

$$\gamma_1 = \gamma_b + \gamma_r + 2\gamma_{se} + \gamma'_1. \quad (6)$$

Similarly, the decay of the atomic coherence is determined by

$$\gamma_2 = \gamma_b + \gamma_r + \gamma_{se} + \gamma'_2. \quad (7)$$

The components of these rates are γ_b , the geometric loss rate from the bulb, γ_r , the rate of recombination into molecular hydrogen at the bulb wall (typically very small for properly made wall coatings), γ_{se} , the hydrogen-hydrogen spin-exchange collision rate, and γ'_i which includes all other sources of decay, such as decoherence during wall collisions and effects of magnetic-field gradients.

The geometric escape rate from the bulb is given by $\gamma_b = \bar{v}A/4KV_b$, where $\bar{v} = 2.5 \times 10^5 \text{ cm/s}$ is the mean thermal velocity of atoms in the bulb at the operating temperature of 50 °C, $A = 0.254 \text{ cm}^2$ is the area of the bulb entrance aperture, $V_b = 3000 \text{ cm}^3$ is the bulb volume, and $K \approx 6$ is the Klausing factor [21] which accounts for the effects of a collimating tube at the bulb entrance. The spin-exchange rate is given approximately by [18,22]

$$\gamma_{se} = \frac{1}{2}n\bar{v}_r\sigma, \quad (8)$$

where $\bar{v}_r = 3.6 \times 10^5 \text{ cm/s}$ is the mean relative velocity of atoms in the bulb and $\sigma = 21 \times 10^{-16} \text{ cm}^2$ is the hydrogen-

hydrogen spin-exchange cross section at 320 K. The hydrogen density in all levels of the ground state is given by [18,22]

$$n = \frac{I_{tot}}{(\gamma_b + \gamma_r)V_b}, \quad (9)$$

where I_{tot} is the total flux of hydrogen atoms into the storage bulb.

The atomic line- Q is related to the transverse relaxation rate and the maser oscillation angular frequency ω by [17]

$$Q_l = \frac{\omega}{2\gamma_2}. \quad (10)$$

We measure Q_l using the cavity pulling of the maser frequency: neglecting spin-exchange shifts, the maser angular frequency (with the cavity tuned near the atomic hyperfine frequency) is given by [17]

$$\omega = \omega_{24} + \frac{Q_C}{Q_l}(\omega_C - \omega_{24}), \quad (11)$$

where Q_C is the loaded quality factor of the cavity given by $Q_C = \omega_C / \Delta\omega_C$ with $\Delta\omega_C$ the cavity angular frequency full width at half maximum of absorbed power. By measuring the change in maser frequency ω as a function of cavity frequency setting ω_C , we determine the line- Q and thus γ_2 .

A convenient measure of spin-exchange-independent relaxation in a hydrogen maser is given by [18,22]

$$\gamma_t = [(\gamma_b + \gamma_r + \gamma'_1)(\gamma_b + \gamma_r + \gamma'_2)]^{1/2}. \quad (12)$$

A useful form for the population difference decay rate, in terms of γ_t , is found by combining Eq. (12) with Eqs. (6) and (7):

$$\gamma_1 = \frac{\gamma_t^2}{\gamma_2 - \gamma_{se}} + 2\gamma_{se}. \quad (13)$$

Using Eqs. (7)–(10), we can relate the line- Q to I , the net input flux of the maser atomic population inversion (i.e., the difference between the input flux of atoms in state $|2\rangle$ and those in state $|4\rangle$):

$$\frac{1}{Q_l} = \frac{2}{\omega} \left[\gamma_b + \gamma_r + \gamma'_2 + q \frac{I}{I_{th}} \gamma_t \right]. \quad (14)$$

The threshold flux required for maser oscillation (neglecting spin exchange) is given by

$$I_{th} = \frac{\hbar V_C \gamma_t^2}{4\pi\mu_B^2 Q_C \eta}. \quad (15)$$

The maser quality parameter [18,22]

$$q = \left[\frac{\sigma\bar{v}_r \hbar}{8\pi\mu_B^2} \right] \frac{\gamma_t}{\gamma_b + \gamma_r} \left[\frac{V_C}{\eta V_b} \right] \left(\frac{1}{Q_C} \right) \frac{I_{tot}}{I} \quad (16)$$

quantifies the effect of spin exchange on the maser.

The ratio I/I_{tot} is a measure of the effectiveness of the state selection of atoms entering the bulb. While I is not directly measurable, it can be related to the power P radiated by the atoms by [18,22]

$$\frac{P}{P_c} = -2q^2 \left(\frac{I}{I_{th}} \right)^2 + (1-3q) \left(\frac{I}{I_{th}} \right) - 1, \quad (17)$$

where $P_c = \hbar\omega I_{th}/2$. The maser power is also related to the maser Rabi frequency, $|X_{24}| = \mu_{24}\langle H_z \rangle_{bulb}/\hbar$, by [18]

$$P = \frac{I\hbar\omega}{2} \frac{|X_{24}|^2}{\gamma_1 \gamma_2} \left(1 + \frac{|X_{24}|^2}{\gamma_1 \gamma_2} \right)^{-1}, \quad (18)$$

where μ_{24} is the transition magnetic dipole moment coupling the $|2\rangle$ and $|4\rangle$ states (approximately a Bohr magneton at low magnetic fields). The power coupled out of the maser is given by [22] $P_o/P = \beta/(1+\beta)$, where β is the cavity coupling coefficient, given by the ratio of power coupled into the external receiver to internal power loss in the cavity.

If we make the reasonable approximation (given the motional averaging present in our H masers and the careful trimming performed to produce a uniform static magnetic field [17]) that $\gamma'_1 = \gamma'_2 = 0$, then we can determine q and γ_t and therefore quantify the effects of spin exchange and decoherence on the maser. By combining Eqs. (14) and (17) we see

$$\begin{aligned} P &= a_2 \left(\frac{1}{Q_l} \right)^2 + a_1 \left(\frac{1}{Q_l} \right) + a_0, \\ a_2 &= -\frac{E\omega^2}{2}, \\ a_1 &= -\frac{E\omega\gamma_t}{2} \left(1 + \frac{1}{q} \right), \\ a_0 &= -\frac{E\gamma_t^2}{q}, \\ E &= \frac{\hbar^2\omega V_C}{8\pi\mu_B^2 Q_C \eta}. \end{aligned} \quad (19)$$

Thus, by measuring the maser power as a function of inverse line- Q and performing a quadratic fit, we can determine q and γ_t .

In practice, we use this method to determine q and γ_t , then find I_{th} and P_c using Eq. (15) and I from Eq. (17). Under the assumption that $\gamma_t \approx \gamma_b + \gamma_r$ we find I_{tot} from Eq. (16) and n from Eq. (9). The spin-exchange collision rate γ_{se} is found using Eq. (8). Finally, γ_1 is found using Eq. (13) and $|X_{24}|$ is determined from Eq. (18).

C. Zeeman frequency determination

In our test of CPT and Lorentz symmetry, we used a double-resonance technique to make high-precision measurements of the $F=1$, $\Delta m_F = \pm 1$ Zeeman frequency

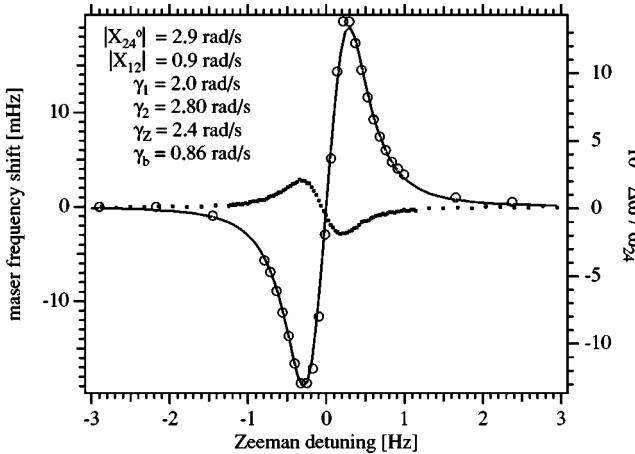


FIG. 3. Examples of double-resonance maser frequency shifts. The large open circles (measured with maser P-8) are compared with Eq. (20) (full curve) using the parameter values shown (see text). The experimental error of each maser frequency measurement (about 40 μ Hz) is smaller than the circle marking it. The solid square data points are data from the CPT/Lorentz symmetry test (maser P-28). Note that the maser frequency shift amplitude for these points was smaller since these data were acquired with a much weaker applied Zeeman field. The large variation of maser frequency with Zeeman detuning near resonance, along with the excellent maser frequency stability, allows the Zeeman frequency (≈ 800 Hz) to be determined to 3 mHz from a single sweep of the resonance (requiring 18 min of data acquisition). The frequency shifts in the two datasets are inverted because maser P-8 operated with an input flux of $|2\rangle$ and $|3\rangle$ atoms, while maser P-28 operated with an input flux of $|1\rangle$ and $|2\rangle$ atoms (see Sec. V C).

[15,23,24]. We applied an oscillating magnetic field perpendicular to the maser's quantization axis, at an audio frequency ω_a , swept this frequency through the atomic Zeeman transition, and measured a dispersionlike shift in the maser frequency (Fig. 3). When the applied field is near the Zeeman frequency, two-photon transitions (one audio photon plus one microwave photon) link states $|1\rangle$ and $|3\rangle$ to state $|4\rangle$, in addition to the single microwave photon transition between states $|2\rangle$ and $|4\rangle$. If there is a difference in the population of atoms in state $|1\rangle$ and state $|3\rangle$, then the two-photon coupling shifts the maser frequency antisymmetrically with respect to the detuning of the applied audio field from the Zeeman resonance [15,23,24]. The large relative variation of the maser frequency with the applied audio field frequency, along with the excellent frequency stability of a hydrogen maser, allows the Zeeman frequency to be determined to ≈ 1 mHz.

We note that the standard method in hydrogen masers for determining the average static magnetic-field strength, and thus the Zeeman frequency, is to scan the Zeeman resonance with a large amplitude oscillating magnetic field and record the reduced maser power (e.g., see Fig. 4, open circles). From the applied field frequency which yields the minimum maser power, typically at the center of a "power resonance" with a width of about 1 Hz, the magnetic field can be found with a resolution of a fraction of 1 μ G and the average Zeeman frequency can be determined to about 0.1 Hz.

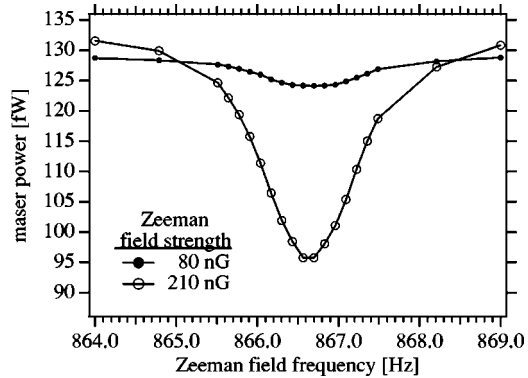


FIG. 4. Maser power reduction due to an applied Zeeman field in maser P-28. The open circles, taken with an applied Zeeman field strength of about 210 nG, represent typical data for the standard "power resonance" method used to determine the static magnetic field in the maser bulb. The filled circles are maser power curves for an applied Zeeman field strength of about 80 nG. Our CPT/Lorentz symmetry test data were taken using the double-resonance technique with a field strength of about 50 nG, inducing a power reduction of less than 2%. These field strengths were determined by fitting the power line shape [15] and extracting the transverse field Rabi frequency $X_{12}=(1/\sqrt{2})\mu_B H_T/\hbar$.

The double-resonance maser frequency shift, in the small static-field limit, ignoring spin exchange, and to second order in the Rabi frequency of the applied audio field, $|X_{12}|$, is given by [15]

$$\begin{aligned} \Delta\omega = & -|X_{12}|^2(\rho_{11}^0 - \rho_{33}^0) \frac{\delta(\gamma_1\gamma_2 + |X_{24}^0|^2)(\gamma_Z/\gamma_b)}{(\gamma_Z^2 - \delta^2 + \frac{1}{4}|X_{24}^0|^2)^2 + (2\delta\gamma_Z)^2} \\ & + |X_{12}|^2 \left(\frac{\omega_C - \omega_{24}}{\omega_{24}} \right) \frac{Q_C\gamma_Z(1+K)}{\gamma_Z^2(1+K)^2 + \delta^2(1-K)^2} \\ & - |X_{12}|^2 \left\{ \frac{\delta(1-K)}{\gamma_Z^2(1+K)^2 + \delta^2(1-K)^2} \right. \\ & \left. - \frac{(\delta+\tau)(1-K)}{\gamma_Z^2(1+K)^2 + (\delta+\tau)^2(1-K)^2} \right\}. \end{aligned} \quad (20)$$

Here γ_Z is the Zeeman decoherence rate, $\delta = \omega_a - \omega_{23}$ is the detuning of the applied audio frequency field from the atomic Zeeman frequency, $\tau = \omega_{23} - \omega_{12}$ is the splitting between the two Zeeman frequencies, $|X_{24}^0|$ is the maser Rabi frequency in the absence of the applied audio field, $K = \frac{1}{4}|X_{24}^0|^2/(\gamma_Z^2 + \delta^2)$, and $\rho_{11}^0 - \rho_{33}^0$ is the steady-state population difference between states $|1\rangle$ and $|3\rangle$ in the absence of the applied audio field. For perfect state selection (i.e., 50% of the H atoms entering the bulb in state $|1\rangle$ and 50% in state $|2\rangle$), this population difference is $\rho_{11}^0 - \rho_{33}^0 = \gamma_b/(2\gamma_1)$. The first term in Eq. (20) results from coherent two-photon mixing of the $F=1$ levels as described above [24], while the second term is a modified cavity pulling term which results from the reduced line- Q in the presence of the applied audio field. The third term is a small maser frequency shift due to the slight nondegeneracy of the two $F=1$, $\Delta m_F = \pm 1$

Zeeman frequencies, which causes a modest offset of the zero crossing of the double-resonance curve away from the average Zeeman frequency, $\frac{1}{2}(\omega_{12} + \omega_{23})$. (Under typical conditions for maser P-8, the zero-crossing offset was $\approx +1.5$ mHz.) All terms in Eq. (20) were included in our fits to the double-resonance data to determine the Zeeman frequency (see Sec. V A below). For example, we compared Eq. (20) to experimental data from maser P-8, inserting the independently measured values of $|X_{24}^0|$, γ_b , γ_1 , and γ_2 (determined as in Sec. IV B). By matching the fit to the data we extracted the parameters $|X_{12}|$ and γ_Z listed in Fig. 3 and Table II, as well as the Zeeman frequency ω_{23} .

An analysis of the double-resonance maser shift which included the effects of spin-exchange collisions [23] showed that there is an additional hydrogen-density-dependent offset of the zero crossing of the maser shift resonance from the average Zeeman frequency. Using the full spin-exchange corrected formula for the maser frequency shift, we calculated this offset and found that for typical hydrogen maser densities ($n \approx 3 \times 10^{15}$ m $^{-3}$), the offset varied with average maser power as ≈ -50 μ Hz/fW (assuming a linear relation between maser power and atomic density of $\Delta P/\Delta n \approx 100$ fW/ 3×10^{15} m $^{-3}$). For typical maser powers of ≈ 100 fW, there is thus a spin-exchange shift of about -5 mHz in the average Zeeman frequency. However, as described below, our masers typically have sidereal power fluctuations of less than 1 fW, making variations in the spin-exchange Zeeman frequency shift negligible for the test of *CPT* and Lorentz symmetry.

By driving the $F=1$, $\Delta m_F = \pm 1$ Zeeman transitions, the applied field depletes the population of the upper maser state $|2\rangle$, thereby diminishing the number of atoms undergoing the maser transition and reducing the maser power (see Fig. 4). Also, by decreasing the lifetime of atoms in state $|2\rangle$, the line- Q is reduced. We found that a very weak applied audio field of about 50 nG (as used in our *CPT*/Lorentz symmetry test) decreases the maser power by less than 2% on resonance and reduces the line- Q by 2% (as calculated using Eq. (6) of Ref. [15]).

V. EXPERIMENTAL PROCEDURE

A. Zeeman frequency measurement

In the test of *CPT* and Lorentz symmetry, we repeatedly measured the atomic hydrogen $F=1$, $\Delta m_F = \pm 1$ Zeeman frequency using the hydrogen maser double-resonance technique. As described above, an applied audio-frequency magnetic field (of peak amplitude about 50 nG) shifted the maser frequency in a dispersivelike manner by a few millihertz (at the extrema), a fractional shift of about 2 parts in 10^{12} . The frequency of the perturbed maser (P-28) was compared to the frequency of a reference, unperturbed, hydrogen maser (P-13). Because of the excellent fractional frequency stability of the masers (2 parts in 10^{14} over averaging times of 10 s), the shift was easily resolved (see the solid square data points in Fig. 3).

Independent voltage controlled crystal oscillators were phase locked to the signals from the two masers. The output

frequencies of the two oscillators were set by tunable synthesizers as part of heterodyne receivers for each maser, such that there was about a 1.2-Hz offset between the oscillators. The two output signals were combined in a double-balanced mixer and the resulting beat note (period ≈ 0.8 s) was measured for 10 s (about 12 periods) with a frequency counter. Typically we made 100 relative maser frequency measurements to determine a double-resonance spectrum with 80% of the points in the middle 40% of the scan range, where the frequency shift varied the most.

Each double-resonance spectrum of beat period (i.e., maser frequency) vs applied audio field frequency was fit to the function described by Eq. (20) to determine the hydrogen Zeeman frequency ν_Z . For example, the solid square data points of Fig. 3, measured with maser P-28, led to an uncertainty in the Zeeman frequency of 3 mHz. For the weak driving field employed in this case, the amplitudes of the frequency-symmetric terms in Eq. (20) were consistent with zero. The fitted parameters of the antisymmetric term allow us to further characterize the maser. Using $\gamma_b = 0.86$ rad/s (determined geometrically) and $\gamma_2 = 2.3$ rad/s (determined from the line- Q), we found that $X_{24}^0 = 2.1$ rad/s, $\gamma_1 = 1.1$ rad/s, and $\gamma_Z = 2.4$ rad/s. (Because the symmetric shift terms were not resolvable in this measurement, we chose $X_{12} = 0.3$ rad/s for maser P-28 such that the ratio of the square of X_{12} for P-28 to that for P-8 was equal to the ratio of the measured maser shift amplitudes for P-28 and P-8, as shown in Fig. 3.)

To optimize the Zeeman frequency resolution of our experimental procedure, we recorded several double-resonance spectra with 50, 100, and 150 points at both 5-s and 10-s averaging. As the total length of the scans increased, the resolution improved and converged to a limit of around 2.5 mHz. For long acquisition times, the resolution began to degrade due to long-term drift of the Zeeman frequency. (As will be described below, we found that the Zeeman frequency exhibited slow drifts of about 10–100 mHz/day.) We therefore chose a scan of 100 points at 10-s averaging, i.e., a total acquisition time of about 18 min, for each double-resonance spectrum obtained in the Lorentz symmetry test. The results from a Monte Carlo analysis for this data acquisition procedure indicated a Zeeman frequency resolution of 2.7 mHz (see Fig. 5) for a typical double-resonance spectrum.

B. Data analysis

Our net bound on a sidereal variation of the hydrogen $F = 1$, $\Delta m_F = \pm 1$ Zeeman frequency (ν_Z) combines data from three multiday runs of repeated 18-min Zeeman frequency scans. After every ten scans, 20 min of maser frequency stability data with no applied audio field were taken to track the maser's unperturbed frequency. In addition to our automated acquisition of Zeeman frequency data, we continuously monitored the maser's environment. At every 10-s step, we recorded room temperature, maser cabinet temperature, solenoid current, maser power, and ambient magnetic field. Estimates of systematic effects are discussed in Sec. VI. Each run contained about ten continuous days of data and more

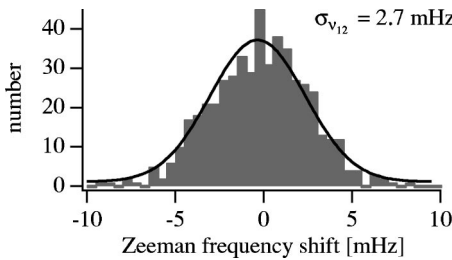


FIG. 5. Results from a Monte Carlo analysis of the resolution of the double-resonance method for determining the hydrogen Zeeman frequency. The horizontal axis represents the variation in extracted Zeeman frequency as determined by fitting synthetic datasets [25]. Each set was constructed by evaluating the fit function (as determined from the data) at each drive frequency and adding Gaussian noise of $40 \mu\text{Hz}$ as determined from the stability of the unperturbed maser. The vertical axis is the number of datasets whose extracted Zeeman frequency lies within each frequency bin. The width of the Gaussian fit to the data is 2.7 mHz , representing the estimated resolution of a Zeeman frequency determination from one double-resonance spectrum.

than 500 Zeeman frequency measurements (e.g., Fig. 6). However, there were periods during which the Zeeman frequency drifted too rapidly to be fit by our model (described below). These periods were cut from the dataset, leaving 19 days of data for analysis.

The Zeeman frequency data, corrected for measured variations in the solenoid current (see Sec. VI A), were fit to a function of the form

$$\begin{aligned} \text{fit} = & a_0 + T \sum_{i=1}^{n-1} a_i + a_n [t - (n-1)T] + \delta\nu_{Z,\alpha} \cos(\Omega t) \\ & + \delta\nu_{Z,\beta} \sin(\Omega t), \end{aligned} \quad (21)$$

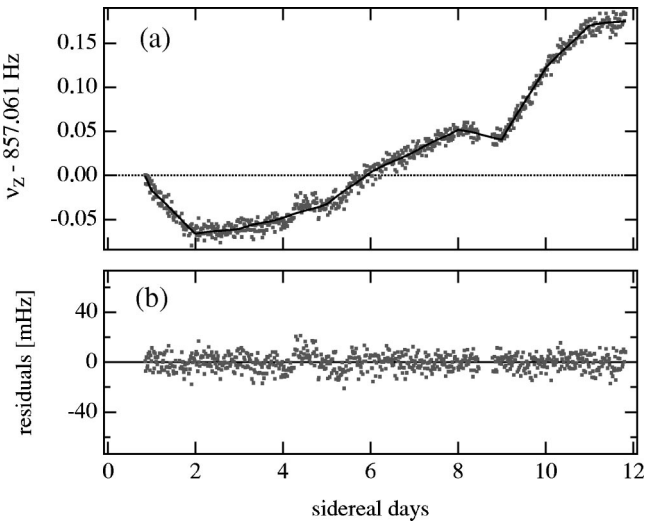


FIG. 6. (a) Analyzed hydrogen Zeeman frequency data from run 1 (November, 1999) and the corresponding fit function (solid line). From the measured Zeeman frequencies, we subtracted the initial value 857.061 Hz and the effect of measured solenoid current variations. (b) Residuals after fitting the data to Eq. (21); i.e., the difference between the Zeeman frequency data and the fit function.

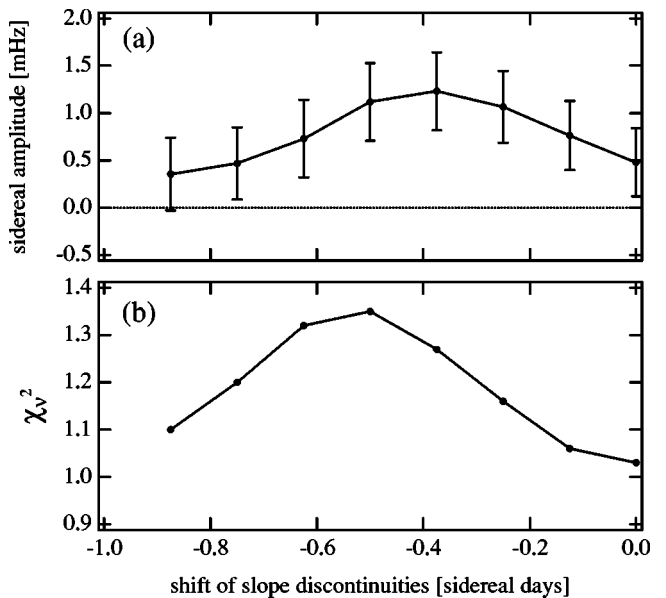


FIG. 7. (a) Total sidereal amplitudes for run 1 data as a function of the time of slope discontinuity locations in the piecewise continuous fit function. (b) Corresponding reduced chi squared (χ^2_ν) parameters. The minimum value occurs with a slope break origin of midnight (00:00) at the beginning of November 19, 1999.

where $\delta\nu_{Z,\alpha}$ and $\delta\nu_{Z,\beta}$ are the amplitudes of the cosine and sine components of the sidereal modulation of the Zeeman frequency, the $\{a_i\}$ are the slopes of a linear function modeling the drift as discussed below [26], and n is the number of sidereal days since the start of the dataset. The period and angular frequency associated with a sidereal day are referred to as T and Ω , respectively. The subscripts α and β refer to two nonrotating orthogonal axes perpendicular to the rotation axis of the Earth. The total amplitude of a sidereal-period modulation of ν_Z was determined by adding $\delta\nu_{Z,\alpha}$ and $\delta\nu_{Z,\beta}$ in quadrature. During each run, the Zeeman frequency drifted hundreds of millihertz over tens of days. The linear function in Eq. (21), with piecewise continuous derivatives and segments of one sidereal day in length, was included to account for these long-term Zeeman frequency drifts without obscuring any potential sidereal variations. This function was continuous at each break, while the derivative was discontinuous. The result of the above analysis procedure was in good agreement with a second analysis method in which each day of Zeeman frequency data was fit to a line plus the sidereal-period sinusoid, and the cosine and sine amplitudes for all days were averaged separately and then combined in quadrature to find the total sidereal-period amplitude.

To avoid a biased choice of fitting, we varied the times of the slope discontinuities in the piecewise continuous linear function throughout a sidereal day. We made eight separate fits, each with the times of the slope discontinuities shifted by three sidereal hours. The total sidereal-period amplitude and reduced chi squared (χ^2_ν) for these eight fits are shown in Fig. 7. We chose our result from the fit with minimum χ^2_ν .

The cumulative data from the first run (November, 1999) are shown in Fig. 6(a) and the residuals from the fit to Eq. (21) are shown in Fig. 6(b). This run consisted of 11 full

days of data and had an overall Zeeman frequency drift of about 250 mHz.

As noted above, the uncertainty in a single Zeeman frequency determination was about 3 mHz. However, when analyzing a typical day of Zeeman frequency data we found a residual rms fluctuation of about 5 mHz. We believe this discrepancy in short- and long-term Zeeman frequency determination is due mainly to residual thermal fluctuations, as discussed in Sec. VII B.

In run 1, for the choice of slope discontinuity with minimum χ^2_ν , the sidereal cosine amplitude was $\delta\nu_{Z,\alpha} = 0.43 \text{ mHz} \pm 0.36 \text{ mHz}$, and the sidereal sine amplitude was $\delta\nu_{Z,\beta} = -0.21 \text{ mHz} \pm 0.36 \text{ mHz}$. The total sidereal-period amplitude for run 1 was therefore $|\delta\nu_Z| = \sqrt{\delta\nu_{Z,\alpha}^2 + \delta\nu_{Z,\beta}^2} = 0.48 \text{ mHz} \pm 0.36 \text{ mHz}$ [27]. Note that this total amplitude is, by definition, positive, with the most probable value (for a normal distribution) equal to one standard deviation.

C. Field-inverted runs

In runs 2 and 3, the static solenoid magnetic-field orientation was opposite to that of the initial run, which enabled us to investigate potential systematics associated with the solenoid field. With the static field inverted, and therefore directed opposite to the quantization axis at the exit of the state selecting hexapole magnet, the input flux consisted of atoms in states $|2\rangle$ and $|3\rangle$ (rather than states $|1\rangle$ and $|2\rangle$). Thus, reversing the field inverted the steady-state population difference ($\rho_{11}^0 - \rho_{33}^0$) of Eq. (20) and acted to invert the antisymmetric double-resonance maser frequency shift [15,23,24].

Operating the maser in the field reversed mode also degraded the maser frequency stability and hence the Zeeman frequency measurement sensitivity [see Figs. 8(a) and 9(a)]. With opposed quantization fields inside the maser bulb and at the exit of the state selecting hexapole magnet, a narrow region of field inversion was created. Where the field passed through zero, Majorana transitions between the different m_F sublevels of the $F=1$ manifold could occur. This reduced the number of atoms in the upper maser state ($F=1, m_F=0$, state $|2\rangle$), diminishing the overall maser power (by $\approx 30\%$ in maser P-28) and degrading the frequency stability. In addition, the overall Zeeman frequency drift was larger in runs 2 and 3 (nearly 800 mHz over about 10 days) than in run 1; also, the scatter in the Zeeman frequency data was increased, as can be seen from the residual plots in Figs. 8(b) and 9(b) which are displayed with the same scale as the residuals from the first run [Fig. 6(b)].

Furthermore, the field-inverted data suffered from more changes of the slope of long-term Zeeman frequency drift (often on time scales less than 1 day) than did the first run. Therefore, less of the data could be analyzed with our model [Eq. (21)] while maintaining $\chi^2_\nu \approx 1$: only 3 of 10 days of run 2 (see Fig. 8) and 5 of 12 days in run 3 (see Fig. 9) passed this analysis criterion. As a result, bounds on sidereal-period amplitudes from runs 2 and 3 were up to an order of magnitude less stringent than for the first run. All values are shown together in Table III.

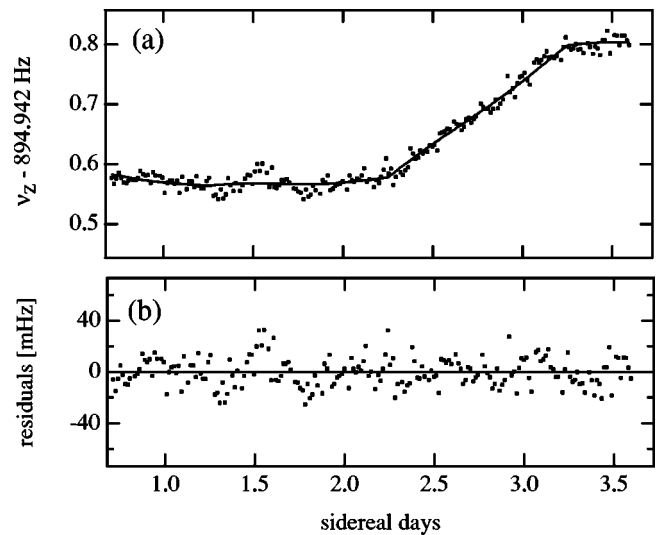


FIG. 8. (a) Analyzed hydrogen Zeeman frequency data from run 2 (December, 1999) and the corresponding fit function (solid line). From the measured Zeeman frequencies, we subtracted the initial value 894.942 Hz and the effect of measured solenoid current variations. (b) Residuals after fitting the data to Eq. (21); i.e., difference between the Zeeman frequency data and the fit function.

We calculated a bound on the total amplitude of sidereal variation of the $F=1, \Delta m_F=\pm 1$ hydrogen Zeeman frequency by adding in quadrature the weighted mean cosine and sine amplitudes from all three runs ($\delta\nu_{Z,\alpha}$ and $\delta\nu_{Z,\beta}$) after accounting for the sign reversal due to the magnetic-field inversion in the raw data: $A = \sqrt{\delta\nu_{Z,\alpha}^2 + \delta\nu_{Z,\beta}^2} = 0.49 \pm 0.34 \text{ mHz}$. As noted above, such an amplitude must be positive, with its most probable value equal to one standard deviation, assuming a normal distribution.

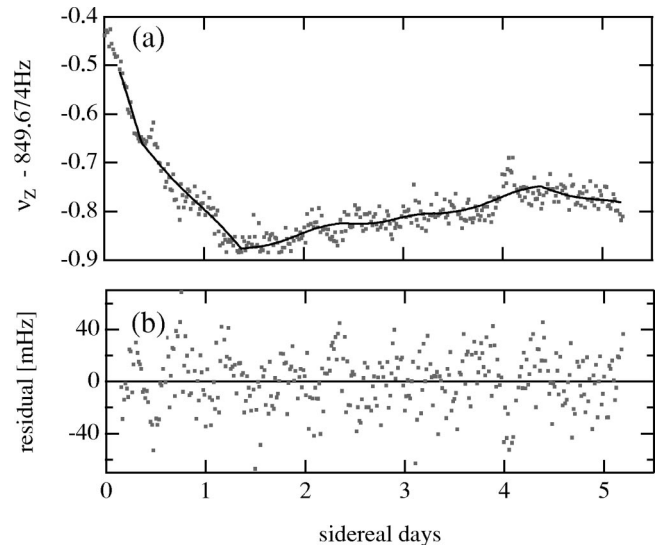


FIG. 9. (a) Analyzed hydrogen Zeeman frequency data from run 3 (March, 2000) and the corresponding fit function (solid line). From the measured Zeeman frequencies, we subtracted the initial value 849.674 Hz and the effect of measured solenoid current variations. (b) Residuals after fitting the data to Eq. (21); i.e., difference between the Zeeman frequency data and the fit function.

TABLE III. Amplitudes of sidereal variations in the hydrogen Zeeman frequency for both quadratures ($\delta\nu_{Z,\alpha}$ and $\delta\nu_{Z,\beta}$) from all runs. [See Eq. (21).]

| Run | $\delta\nu_{Z,\alpha}$ (mHz) | $\delta\nu_{Z,\beta}$ (mHz) |
|-----|------------------------------|-----------------------------|
| 1 | 0.43 ± 0.36 | -0.21 ± 0.36 |
| 2 | -2.02 ± 1.27 | -2.75 ± 1.41 |
| 3 | 4.30 ± 1.86 | 1.70 ± 1.94 |

VI. SYSTEMATICS AND ERROR ANALYSIS

A. Magnetic-field systematics

The $F=1$, $\Delta F=\pm 1$ atomic hydrogen Zeeman frequency depends to first order on the z component of the magnetic field in the storage bulb. Thus, all external field variations must be sufficiently screened to enable high sensitivity to possible frequency shifts from *CPT* and Lorentz symmetry violation. In our hydrogen masers the maser cavity and bulb are surrounded by a set of four nested magnetic shields (made of high permeability metal), which reduce the z component of the ambient field by a factor of $\approx 32\,000$ for uniform fields. We measured unshielded fluctuations in the ambient magnetic field of about 3 mG (peak-peak) throughout any given day, and even when shielded these fluctuations added significant noise to each Zeeman frequency determination using the double-resonance technique, as illustrated in Fig. 10(a). Furthermore, the amplitude of the field fluctuations was significantly reduced late at night, due to the cessation of local subway and electric bus lines. These nightly

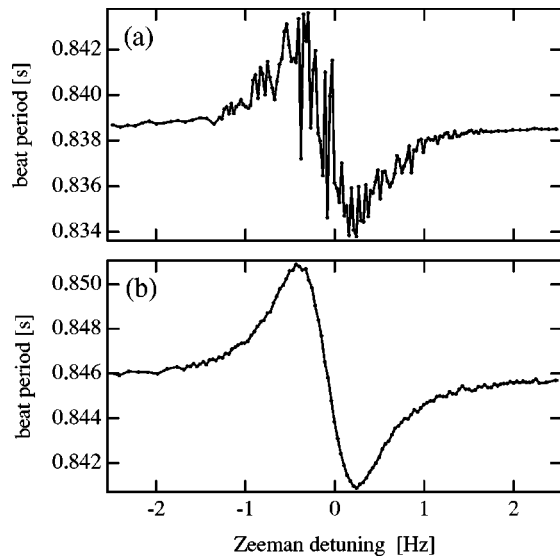


FIG. 10. (a) Double-resonance “Zeeman scan” without active compensation for ambient magnetic-field fluctuations. The “noise” on the scan is due to shifting of the antisymmetric resonance as the hydrogen Zeeman frequency is changed by ambient field fluctuations (magnitude about 3 mG outside the shields). (b) Zeeman scan with active compensation for ambient magnetic-field fluctuations using a Helmholtz coil feedback loop. Ambient field fluctuations outside the maser’s passive magnetic shields were effectively reduced to less than 5 μ G.

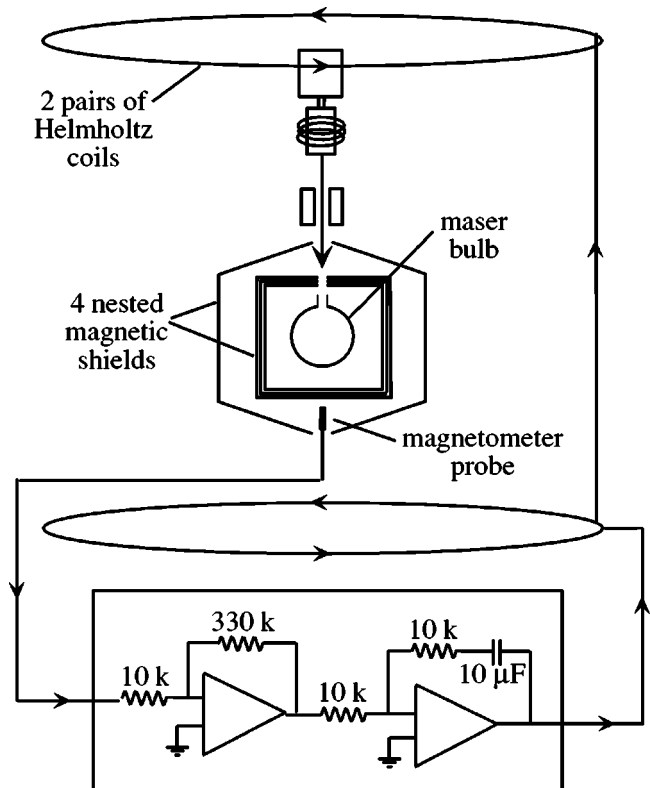


FIG. 11. Schematic of the active system used to compensate for ambient magnetic-field fluctuations. A large set of Helmholtz coils (50 turns) canceled all but a residual (~ 5 mG) z component of the ambient field. This residual field, detected with a fluxgate magnetometer probe, was actively canceled by a servoloop and a second pair of Helmholtz coils (three turns). The servoloop consisted of a proportional stage (gain of 33), an integral stage (time constant of 0.1 s), and a derivative stage (time constant of 0.01, not shown). The overall time constant of the loop was about $\tau=0.1$ s.

reductions in fluctuations could have generated a diurnal (24 h) systematic effect in our data which would have been difficult to distinguish from a sidereal (23.93 h) signal.

To reduce the effect of ambient magnetic-field variations, we installed an active feedback system (see Fig. 11) consisting of two pairs of large Helmholtz coils (each 2.4 m diameter) and a fluxgate magnetometer. The magnetometer probe was placed inside the maser’s outermost magnetic shield near the maser cavity. Due to its location inside one magnetic shield, the probe was shielded by a factor of about 6 from external fields, producing a differential shielding of 5300 between the magnetometer probe and the hydrogen atoms in the maser storage bulb. The first pair of Helmholtz coils (50 turns per coil) produced a uniform, static magnetic-field to cancel all but 5 mG of the z component of the ambient field. The magnetometer output controlled a second Helmholtz coil pair (three turns per coil) via a PID servoloop which canceled the residual field and actively countered any fluctuations. The overall time constant of this ambient field control system was ≈ 0.1 s, i.e., about 100 times shorter than the averaging time of our typical maser frequency measurements (10 s).

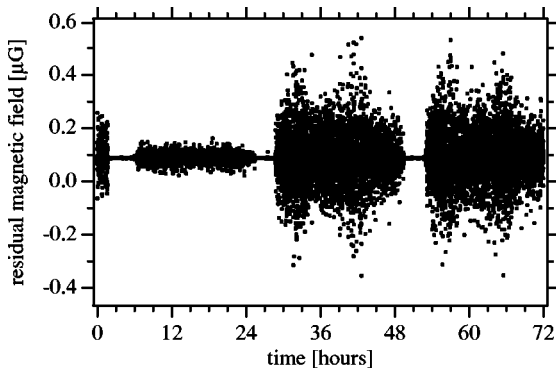


FIG. 12. Residual ambient magnetic-field, after cancellation by the active control loop, as sensed by the magnetometer probe located within the maser's outermost magnetic shield. Each point is a 10-s average. These three days of typical data depict a Sunday, Monday, and Tuesday, with the time origin corresponding to 00:00 Sunday. From these data it can be seen that for 3 h every night the magnetic noise dies out dramatically due to subway and electric bus cessation, and that the noise level is significantly lower on weekends than weekdays. Nevertheless, with the active feedback system, even the largest fluctuations ($1\text{-}\mu\text{G}$ peak-peak) caused changes in the hydrogen Zeeman frequency that were below our sensitivity ($\Delta B = 1\text{-}\mu\text{G} \Rightarrow \Delta \nu_Z = 0.3\text{ mHz}$).

With this system we were able to reduce ambient magnetic-field fluctuations at the magnetometer by a factor of 1000 beyond the passive screening provided by the metallic magnetic shields. The resulting measured field fluctuations at the magnetometer position within the outermost magnetic shield were less than $1\text{-}\mu\text{G}$ peak-peak (see Fig. 12). Induced fluctuations on the maser frequency due to residual magnetic fluctuations were thus reduced below our measurement resolution, as shown in Fig. 10(b). During the *CPT* and Lorentz symmetry test, the sidereal component of the magnetic-field variation measured at the probe was $\leq 1\text{ nG}$, corresponding to a shift of less than $0.2\text{ }\mu\text{Hz}$ on the hydrogen Zeeman frequency, i.e., three orders of magnitude smaller than the sidereal Zeeman frequency bound set by our experiment. This small systematic uncertainty in the Zeeman frequency was included in the net error analysis, as described in Sec. VII.

The fluxgate magnetometer could also be sensitive to potential Lorentz-violating interactions through the spin orientation of the electrons in its magnetic core. However, based on the latest bound on electron Lorentz violation (10^{-29} GeV) [12], any Lorentz-violating effect on the magnetometer corresponds to an effective magnetic-field change of less than 10^{-11} G , far below the level of residual ambient field fluctuations. Also, the additional shielding factor of 5300 between the magnetometer probe and the hydrogen atoms further reduced the effect of any Lorentz-violating shift in the probe electrons' energies.

With the z component of the ambient field maintained near zero, the Zeeman frequency was set by the magnetic-field generated by the three-coil maser solenoid assembly, and hence by the solenoid currents. We monitored solenoid current fluctuations by measuring the voltage across the main coil's current-limiting resistor. By measuring the Zeeman

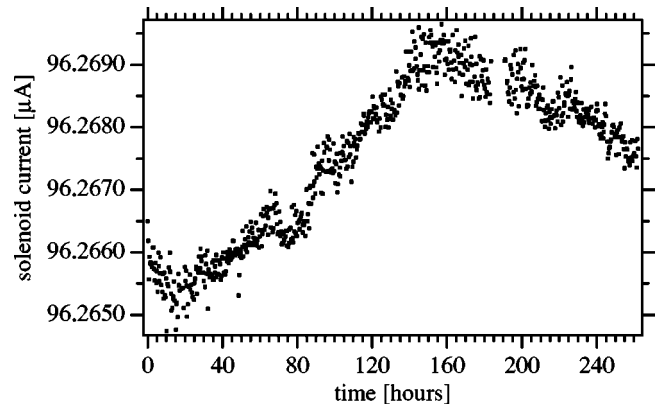


FIG. 13. Maser P-28's solenoid current during the first data run (see Fig. 6). Each point is an average obtained during one full hydrogen Zeeman frequency measurement (18 min). Since the Zeeman frequency is proportional to the solenoid current, we subtracted these solenoid current drifts directly from the raw Zeeman data, using a measured calibration.

frequency shift caused by modest current changes in the main coil, we found a dependence of 8 mHz/nA . Long-term drifts in the current were typically about 5 nA (see Fig. 13), large enough to produce detectable shifts in the Zeeman frequency. We corrected for these drifts directly in the Zeeman data during data analysis using the above current/Zeeman frequency calibration. In particular, the measured sidereal component of the solenoid current variation was $25 \pm 10\text{ pA}$, possibly arising from diurnal temperature variations of the current supply or solenoid assembly. This sidereal current variation corresponded to a sidereal Zeeman frequency variation of $0.16 \pm 0.08\text{ mHz}$. We corrected the Zeeman data for this effect, and included the resultant small systematic uncertainty in the Zeeman frequency in the net error analysis for the Lorentz/*CPT* symmetry test (Sec. VII).

B. Other systematics

During the Lorentz symmetry test, the perturbed, double-resonance hydrogen maser (P-28) and the unperturbed, reference maser (P-13) both resided in a closed room in which the temperature oscillated with a peak-peak amplitude of slightly less than 0.5 K and a period of around 15 min (driven by the room air-conditioning system). The outermost shell of both masers was an insulated cabinet. In addition, the cabinet of maser P-28 was thermally controlled and provided a factor of 10 isolation from temperature fluctuations of the room, as shown in Fig. 14. By changing the temperature within maser P-28's cabinet while measuring the Zeeman frequency, we found a relation of about 200 mHz/K , due mainly to the effect of temperature on the solenoid current source. (As described above, we monitored and corrected for changes in the solenoid current during the *CPT/Lorentz* symmetry test.)

However, remnant temperature-induced changes in P-28's magnetic-field and hence the Zeeman frequency could arise from adjusting currents in the four-layer system of maser temperature control (inside the maser cabinet as well as three other layers of control progressively deeper inside the ma-

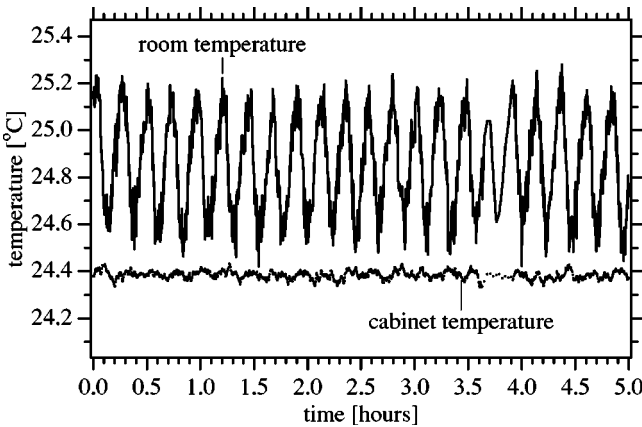


FIG. 14. Temperature data during the first run (see Fig. 6). Each point is a 10 s average. The top trace shows the characteristic 0.5 °C peak-peak, 15 min period oscillation of the room temperature. The bottom trace shows the screened oscillations inside the cabinet of maser P-28. The cabinet is insulated and temperature controlled with a blown air system. (The microwave cavity and storage bulb are further insulated from the maser cabinet air temperature, and independently temperature controlled to 1 mK or better.) The residual temperature variation of the maser cabinet air had a sidereal variation of 0.5 mK, resulting in an additional systematic uncertainty of 0.1 mHz on the hydrogen Zeeman frequency.

ser). On an intermediate time scale of a few hours, we estimate that such temperature-induced effects produced additional variations of about 1 mHz in the measured Zeeman frequency, increasing the estimated error of the mean of the fitted residual Zeeman frequency in a given day from about 3 mHz to 5 mHz. On a longer time scale, our measurements placed a bound of 0.5 mK on the sidereal component of temperature fluctuations directly inside the cabinet (where the solenoid current source resides), which would produce a systematic sidereal variation of 100 μHz on the Zeeman frequency and is included in the net error analysis. This variation is about a factor of 3 smaller than the statistical limit on sidereal variation in Zeeman frequency.

As mentioned in Sec. IV C, spin-exchange effects induce a small offset of the Zeeman frequency, as determined by the double-resonance technique, from the actual Zeeman frequency [23]. Thus, variations in the input atomic flux (and therefore the atomic density and the maser power) could cause variations in the Zeeman frequency measurement. We measured a limit of less than 0.8 mHz/fW on the shift of the Zeeman frequency due to changes in average maser power.

[Expected shifts from spin exchange are ten times smaller than this level (Sec. IV C). We believe that the measured limit is related to heating of the maser as the flux is increased.] During long-term operation, the average maser power drifted by ≈1 fW/day (see Fig. 15). The sidereal component of the variations of the maser power was less than 0.05 fW, implying a systematic sidereal variation in the Zeeman frequency of less than 40 μHz which we included in the net error analysis.

VII. RESULT AND DISCUSSION

We determined systematic errors in our search for a sidereal hydrogen Zeeman frequency variation (as described in

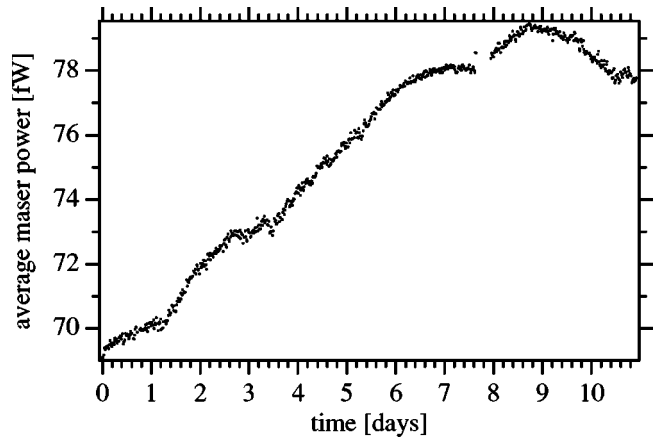


FIG. 15. Average output power of maser P-28 during the first data run. Each point is an average over one full Zeeman frequency measurement (18 min). We measured a sidereal variation in the maser power of less than 0.05 fW, leading to an additional systematic uncertainty in the hydrogen Zeeman frequency of 0.04 mHz, which is included in the net error analysis.

Secs. VI A and VI B) due to the ambient magnetic-field (0.2 μHz), solenoid field (80 μHz), maser cabinet temperature (100 μHz), and hydrogen density effects (40 μHz). Combining these errors in quadrature with the 0.34-mHz statistical uncertainty (see Sec. V C), we determine a final bound on the amplitude A of a sidereal variation of the $F=1$, $\Delta m_F = \pm 1$ Zeeman frequency in hydrogen of $A = 0.44 \pm 0.37$ mHz at the one-standard-deviation level. This 0.37-mHz bound corresponds to 1.5×10^{-27} GeV in energy units.

We note that since the sidereal variation amplitude A is a strictly positive quantity, the present result is consistent with no sidereal variation at the 1- σ level: in the case where $\delta\nu_{Z,\alpha}$ and $\delta\nu_{Z,\beta}$ have zero mean value and the same standard deviation σ , the probability distribution for A takes the form $P(A) = A\sigma^{-2} \exp(-A^2/2\sigma^2)$, which has the most probable value occurring at $A = \sigma$. Our result for A is less than one standard deviation different from this most probable value.

To make meaningful comparisons between our result and other experimental searches for spin couplings to background vector and tensor fields, we interpret our 0.37-mHz bound on a sidereal modulation of the hydrogen Zeeman frequency in terms of a fixed, approximately inertial, reference frame. Following the construction in Ref. [4], we label the fixed frame with coordinates (X, Y, Z) and the laboratory frame with coordinates (x, y, z) , as shown in Fig. 16. We define the frame with the Earth's rotation axis as the Z axis, declination = right ascension = 0° degrees as the X axis, and declination = 0°, right ascension = 90° as the Y axis. With this convention, the X and Y axes lie in the plane of the Earth's equator. Note that the α , β axes of Sec. V B, also in the Earth's equatorial plane, are rotated about the Earth's rotation axis from the X, Y axes by an angle equivalent to the right ascension of 71°7' longitude at 00:00 of November 19, 1999.

For our experiment, the quantization axis (which we denote z) was vertical in the lab frame, making an angle χ

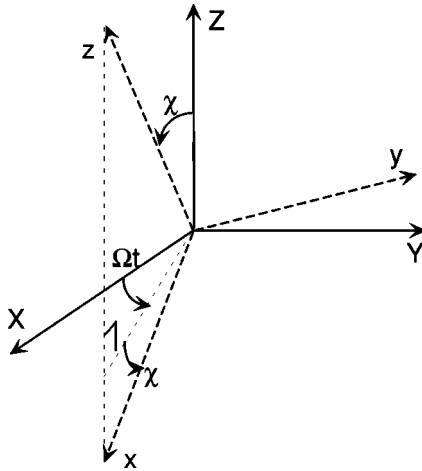


FIG. 16. Coordinate systems used in the interpretation of the current experiment (following the convention of Ref. [4]). Coordinate set (X, Y, Z) refers to a fixed reference frame, and coordinate set (x, y, z) refers to the laboratory frame. The lab frame is tilted from the fixed Z axis by the colatitude of Cambridge, MA ($\approx 48^\circ$), and rotates about Z as the Earth rotates. The α and β axes, described in Sec. V, span a plane parallel to the X - Y plane.

$\approx 48^\circ$ relative to Z , accounted for by rotating the entire (x, y, z) system by χ about Y . The lab frame (x, y, z) rotates about Z by an angle Ωt , where Ω is the (sidereal) rotation frequency of the earth.

These two coordinate systems are related through the transformation matrix

$$\mathbf{T} = \begin{pmatrix} \cos \chi \cos \Omega t & \cos \chi \sin \Omega t & -\sin \chi \\ -\sin \Omega t & \cos \Omega t & 0 \\ \sin \chi \cos \Omega t & \sin \chi \sin \Omega t & \cos \chi \end{pmatrix}. \quad (22)$$

Then, vectors transform as $\vec{b}_{lab} = \mathbf{T} \vec{b}_{fixed}$, while tensors transform as $\mathbf{d}_{lab} = \mathbf{T} \mathbf{d}_{fixed} \mathbf{T}^{-1}$.

As discussed in Sec. III, a possible Lorentz-violating shift in the hydrogen $F=1$, $\Delta m_F = \pm 1$ Zeeman frequency depends on the following combination of terms (for both electron and proton):

$$\tilde{b}_z = b_z - m d_{zt} - H_{xy}. \quad (23)$$

Transforming the components of \tilde{b}_z to the fixed frame, we find

$$\begin{aligned} \tilde{b}_z = & (b_Z - m d_{Z0} - H_{XY}) \cos \chi + (b_Y - m d_{Y0} - H_{ZX}) \\ & \times \sin \chi \sin \Omega t + (b_X - m d_{X0} - H_{YZ}) \sin \chi \cos \Omega t. \end{aligned} \quad (24)$$

The first term on the right is a constant offset, not bounded by our experiment. The second and third terms each vary at the sidereal frequency. Combining Eq. (24) [for both the electron (e^-) and proton (p)] with Eq. (4), we find the magnitude of the sidereal variation of the hydrogen Zeeman frequency:

$$\begin{aligned} |\Delta \nu_Z|^2 = & [(b_Y^e - m_e d_{Y0}^e - H_{ZX}^e) + (b_Y^p - m_p d_{Y0}^p - H_{ZX}^p)]^2 \frac{\sin^2 \chi}{h^2} \\ & + [(b_X^e - m_e d_{X0}^e - H_{YZ}^e) \\ & + (b_X^p - m_p d_{X0}^p - H_{YZ}^p)]^2 \frac{\sin^2 \chi}{h^2}. \end{aligned} \quad (25)$$

Inserting the colatitude $\chi = 48^\circ$, into Eq. (25) and comparing to our experimental limit on $|\delta \nu_Z|$, we obtain

$$\sqrt{(\tilde{b}_X^e + \tilde{b}_X^p)^2 + (\tilde{b}_Y^e + \tilde{b}_Y^p)^2} = (3 \pm 2) \times 10^{-27} \text{ GeV}. \quad (26)$$

Therefore, our experiment sets a one-standard-deviation bound of 2×10^{-27} GeV on the net orientation-dependent effect of Lorentz and *CPT* violation on the proton and electron. Table I provides a comparison of our result with other recent tests of Lorentz and *CPT* symmetry. Although our bounds are numerically similar to those from the $^{199}\text{Hg}/^{133}\text{Cs}$ experiment, the simplicity of the hydrogen atom allows us to place bounds more directly on the electron and proton; in particular, uncertainties in nuclear structure models do not complicate the interpretation of our result. The recent limit of 10^{-29} GeV on electron Lorentz and *CPT* violation set by the torsion pendulum experiment of Adelberger *et al.* [12] casts our result as a clean bound on Lorentz and *CPT* violation of the proton.

To make a more sensitive search for a sidereal variation of the Zeeman frequency in a hydrogen maser, it will be important to identify and reduce the long-term drift of the Zeeman frequency (i.e., on time scales greater than 1 day). Possible sources of these drifts are magnetic-fields near the maser bulb caused by currents in heaters or power supplies in the inner regions of the maser. It will also be important to reduce variation of the Zeeman frequency on time scales of minutes to hours, which we believe is currently caused by thermal fluctuations in the maser and its environment driving local magnetic-field fluctuations. Both of these objectives could be accomplished by carefully rebuilding a hydrogen maser with temperature and other control systems designed to minimize unwanted magnetic-fields applied to the hydrogen atoms, and by operating the maser in a room with improved environmental control. We estimate that these steps, together with greater data taking, will enable an order of magnitude improvement in the Lorentz/*CPT* violation test described here.

ACKNOWLEDGMENTS

We gratefully acknowledge the encouragement of Alan Kostelecký and the technical support of Jim Maddox. Financial support was provided by NASA Grant No. NAG8-1434 and the Smithsonian Institution. M.A.H. acknowledges NASA for financial support under the Graduate Student Researchers Program.

- [1] V.A. Kostelecký and S. Samuel, Phys. Rev. Lett. **63**, 224 (1989); Phys. Rev. D **40**, 1886 (1989); Phys. Rev. Lett. **66**, 1811 (1991).
- [2] V.A. Kostelecký and S. Samuel, Phys. Rev. D **39**, 683 (1989); **40**, 1886 (1989); V.A. Kostelecký and R. Potting, Nucl. Phys. B **359**, 545 (1991); Phys. Lett. B **381**, 89 (1996); V.A. Kostelecký, M.J. Perry, and R. Potting, Phys. Rev. Lett. **84**, 4541 (2000).
- [3] V. A. Kostelecký and R. Potting, in *Gamma Ray-Neutrino Cosmology and Planck Scale Physics*, edited by D.B. Cline (World Scientific, Singapore, 1993); V.A. Kostelecký, R. Potting, Phys. Rev. D **51**, 3923 (1995); D. Colladay and V.A. Kostelecký, *ibid.* **55**, 6760 (1997); **58**, 116002 (1998).
- [4] V.A. Kostelecký and C.D. Lane, Phys. Rev. D **60**, 116010 (1999).
- [5] V.A. Kostelecký and C.D. Lane, J. Math. Phys. **40**, 6245 (1999).
- [6] R. Bluhm, V.A. Kostelecký, and N. Russell, Phys. Rev. Lett. **82**, 2254 (1999).
- [7] D.F. Phillips, M.A. Humphrey, E.M. Mattison, R.E. Stoner, R.F.C. Vessot, and R.L. Walsworth, Phys. Rev. D **63**, 111101(R) (2001).
- [8] Gauge invariance and renormalizability exclude several additional parameters in the standard model extension as described in Sec. II A of Ref. [4]. These parameters are thus omitted here.
- [9] R. Bluhm, V.A. Kostelecký, C.D. Lane, and N. Russell, Phys. Rev. Lett. **88**, 090801 (2002).
- [10] R.K. Mittleman, I.I. Ioannou, H.G. Dehmelt, and N. Russell, Phys. Rev. Lett. **83**, 2116 (1999); H. Dehmelt, R. Mittleman, R.S. Van Dyck, Jr., and P. Schwinberg, *ibid.* **83**, 4694 (1999).
- [11] E.G. Adelberger *et al.*, in *Physics Beyond the Standard Model*, edited by P. Herczeg *et al.* (World Scientific, Singapore, 1999), p. 717; M.G. Harris, Ph.D. thesis, University of Washington, 1998 (unpublished).
- [12] B. Heckel, presented at the International Conference on Orbis Scientiae 1999, Fort Lauderdale, Florida, 1999.
- [13] D. Bear, R.E. Stoner, R.L. Walsworth, V.A. Kostelecký, and C.D. Lane, Phys. Rev. Lett. **85**, 5038 (2000); **89**, 209902(E) (2002).
- [14] C.J. Berglund, L.R. Hunter, D. Krause, Jr., E.O. Prigge, M.S. Ronfeldt, and S.K. Lamoreaux, Phys. Rev. Lett. **75**, 1879 (1995).
- [15] H.G. Andresen, Z. Phys. **210**, 113 (1968).
- [16] J. Vanier and C. Audoin, *The Quantum Physics of Atomic Frequency Standards* (Adam Hilger, Bristol, 1989).
- [17] D. Kleppner, H.M. Goldenberg, and N.F. Ramsey, Phys. Rev. **126**, 603 (1962).
- [18] D. Kleppner, H.C. Berg, S.B. Crampton, N.F. Ramsey, R.F.C. Vessot, H.E. Peters, and J. Vanier, Phys. Rev. **138**, A972 (1965).
- [19] Maser P-28 was available for a restricted period. Maser P-8 is housed permanently in our laboratory, so we could perform more extensive characterization of this maser. Note that maser P-8 was not suitable for a *CPT*/Lorentz symmetry test because it suffered from large, long-term Zeeman frequency drifts, attributed to less effective magnetic shielding and larger extraneous magnetic-fields (e.g., from heating elements), than maser P-28. However, the two masers have very comparable geometries, relaxation rates, and hydrogen sources, making a comparison of the operational parameters useful.
- [20] For further details regarding the characterization of these masers, see M.A. Humphrey, Ph.D. thesis, Harvard, 2003 (unpublished).
- [21] N.F. Ramsey, *Molecular Beams* (Clarendon Press, Oxford, 1956).
- [22] E.M. Mattison, W. Shen, and R.F.C. Vessot, in *Proceedings of the 39th Annual Frequency Control Symposium* (IEEE, New York, 1985), p. 72.
- [23] J.-Y. Savard, G. Busca, S. Rovea, M. Desaintfuscien, and P. Petit, Can. J. Phys. **57**, 904 (1979).
- [24] M.A. Humphrey, D.F. Phillips, and R.L. Walsworth, Phys. Rev. A **62**, 063405 (2000); **63**, 059901(E) (2001).
- [25] W.H. Press, S.A. Teukolsky, W.T. Vetterling, and B.P. Flannery, *Numerical Recipes in C*, 2nd ed. (Cambridge University Press, Cambridge, 1988), p. 689.
- [26] The time origin of the sinusoids for all three runs was taken as midnight (00:00) of November 19, 1999.
- [27] Had we chosen the slope discontinuity with maximum χ^2_ν , the total sidereal amplitude for this run would have been $1.1 \text{ mHz} \pm 0.4 \text{ mHz}$.